A shell-dynamics model for marine pipelines of large suspended length

Stefanos A. Katifeoglou and Ioannis K. Chatjigeorgiou[*]

School of Naval Architects, Division of Marine Structures, National Technical University of Athens, 9 Heroön Polytechniou Ave, GR157-73, Zografos Campus, Athens, Greece

Abstract.   The present investigations introduce the shell-finite element discretization for the dynamics of slender marine pipelines. A long catenary pipeline, corresponding to a particular Steel Catenary Riser (SCR), is investigated under long-standing cyclic loading. The long structure is divided into smaller tubular parts which are discretized with 8-node planar shell elements. The transient analysis of each part is carried out by the implicit time integration scheme, within a Finite Elements (FE) solver. The time varying external loads and boundary conditions on each part are the results of a prior solution of an integrated line-dynamics model. The celebrated FE approximation can produce a more detailed stress distribution along the structural surface than the simplistic "line-dynamics" approach.

1. Introduction

The fatigue damage of long, slender marine pipelines due to long-standing transient loading is one of the most important issues in the offshore engineering industry. Current-induced vibrations of free span pipelines, touchdown motions which induce large soil-reaction forces and oscillating motions of the top-end of risers are some of the most severe transient loading factors. Especially, the Steel Catenary Riser (SCR) is a structure of intensively varying curvature which can perform strongly nonlinear responses along its suspended part when subjected to the aforementioned conditions.

The design guidelines for SCRs (American Petroleum Institute, 1998) refer to line-dynamics treatments of such slender structures in time-domain, implying line-element (rod, beam, pipe, etc.) discretization of the dynamic equilibrium system. Nowadays there are a number of important contributions that have been published regarding SCR transient line-dynamics analyses, via Finite Element Methods, Finite Difference schemes or Lumped Mass approximations. Among the plethora of relevant studies some indicative reports are those due to Chai *et al*. (2002), Meng and Chen (2012) and Chatjigeorgiou (2010a). In the recent years, more and more complex contributions alike the soil reaction force and Vortex Induced Vibrations (e.g., Nakhaee and Zhang 2010, Katifeoglou and Chatjigeorgiou 2012, Riveros *et al*. 1999) or nonlinear tensioner modeling

---

∗Corresponding author, Professor, E-mail: chatzi@naval.ntua.gr

such as the case reported by Huang *et al.* (2013) are taken into account within global dynamics solutions. Furthermore, integrated hull-mooring-SCR coupling reports are also desired in order to clarify the behavior of the complex marine infrastructure. Eom *et al.* (2014) have recently performed such simulations which focused in the local buckling of the touchdown region of a SCR model. Nevertheless, more detailed dynamic simulations of the shell-like SCR, e.g. by employing shell-elements have not yet been extensively reported. The present effort aims at investigating the "shell-dynamics" concept by partially modeling the tubular sections that assemble the whole sagbend region of a deepwater SCR up to its Touch-Down Point (TDP).

2. Description of the physical problem and the FE approach

All tubular pipelines of circular diameter, including the SCRs, can be considered as shell-structures of particular thickness. It is evident that an appropriate FE treatment with planar shell elements can provide more clear and dense information on the spatial distribution of stresses throughout the structural domain than a line-element treatment that can focus only at particular lengthwise nodes. Arabzadeh and Zeinoddini (2011) recently employed a 4-node shell FEM to simulate the dynamics of a submerged pipe at the Touch-Down Zone (TDZ) under impact loads. Hosseini Korkdheili and Bahai (2008) examined statically a riser-soil interaction problem by employing a pipe-elbow FEM in which they introduced an additional membrane-shell intensive behavior. According to the latter developments, it is obvious that more detailed depictures of the stress condition are desired, at least at particular locations of submerged pipes and succinctly, FE shell discretization can provide this information. However, there haven't been any worth mentioning attempts yet as regards the transient analyses of SCR regions under long-standing excitations with equivalently detailed discretization schemes, namely extending the celebrated "line-dynamics" approach to "shell-dynamics".

In addition, the SCRs are virtually relatively large thickness structures in order to resist against large external pressures induced by the marine environment (Kyriakides and Corona 2007). Also, the severity of the bending and the buckling-like deformations at the lower sagbend region due to the boundary conditions at the TDP has been identified as a severe impact of paramount importance. These factors are mainly responsible for the amplification of the local bending moments and shear stresses when the SCR is set into cyclic motion induced by the floater where the top-end of the pipe is attached, and this is considered as a principal transient problem for SCRs.

The above features were the main motive to produce the celebrated the FEM analysis of the sagbend region of a particular deep-water SCR, discretized with planar shells. The parameters of the physical problem are: suspended length L=2024 m, external diameter D=0.429 m and large thickness h=0.022 m (D/h~20). The riser is installed at 1800m water depth under a pretension of 1860 kN. Accordingly, the static analysis of the concerned structure estimates the length of the sagbend region to approximately 594 m. The physical and the mechanical properties of the steel structure are material density 7800 kg/m^3 and Young's modulus of elasticity 207 GPa. In addition, the kinematic boundary and load conditions required for implementing the FE model are introduced as time series of the velocities and the internal loading components which have been primarily derived by an efficient "line-dynamics" model.

According to Bathe and Dvorkin (1986) the most appropriate finite elements for thick-shell structures, such as the particular pipeline, as well as for nonlinear problems and solutions that

require convergence, are the 8-node planar shells. Regarding the time-discretization scheme of the resulting equations, the unconditionally stable Implicit/Newmark method usually performs better for "inertial"/long-duration problems (Subbaraj and Dokainish 1989, Bathe 1979, Bathe 1996). For large deformation analyses (large displacements) and strongly varying internal loads alike the current case, the nonlinear formulation of the Newmark method should be employed (see e.g., Subbaraj and Dokainish 1989). The strong stability characteristics of the concerned method allow the employment of relatively large time discretization (Δt) for convergence. However, the adopted succession for the temporal intervals should be small enough for reasons of accuracy. The calculations which we performed in the context of the present study were based on the information of the previously mentioned studies (Subbaraj and Dokainish 1989, Bathe 1979). All numerical simulations were performed within the ANSYS Workbench 13.0 environment (ANSYS, 2007).

The adopted shell element dimensions for the FEM mesh were 0.1×0.1×h (see Fig. 1), where h stands for the shell's thickness. This resulted into approximately 100,000 elements and accordingly, into an equal number of differential equations. Based on this figure it is easy to realize the required computational capacity for the numerical simulations, taking additionally into account the eight nodes for each element, the time integration steps and the iterations which are needed for convergence. Clearly, such an approach requires enormous memory resources, whilst the time required for achieving the computations would be indeterminately large. Hence a further discretization of the sagbend region into 25 smaller pipe-segments (23.762 m long) was assumed and each of these segments was investigated individually. According to the considered configuration each segment extends between two successive nodes of the FD "line-dynamics" analysis (Fig. 2).

3. Modeling the FE tubular parts

3.1 Description of the "line-dynamics" model

The present FE analysis of the shell tubular members along the sagbend region of a catenary riser relies on the knowledge of their kinematical details. These are determined via the "line-dynamics" approach which relies on the solution of the dynamic equilibrium system of the catenary pipeline, the latter being considered as a continuous elastica. To this end, the governing dynamic system that is composed by a set of partial differential equations (PDEs) must be treated. For the purposes of the present study the Newtonian derivation procedure which is described in Chatjigeorgiou (2010a, b, 2013) has been adopted. The cited publications outline in detail the methodology and eventually the final mathematical system that governs the 3D "line-dynamics" of catenary pipelines conveying an internal fluid without considering the torsion effects. Here we advance one step further by including torsion, which as discussed in the sequel requires a special numerical treatment. In addition, the inner flow effects have been omitted by our contemporary approach as they have admittedly a marginal effect. To support that statement reference is made to the works due to the present authors (Chatjigeorgiou 2010a, Chatjigeorgiou 2013, Katifeoglou *et al*. 2012) who showed that the inner flow, approximated alternatively by (i) the "plug-flow" model (Chatjigeorgiou 2010a), (ii) a potential theory model (Chatjigeorgiou 2010b) and (iii) a fully turbulent flow model (Katifeoglou *et al*. 2012), has negligible effects on the structural behavior of the pipeline. The authors reported some differentiations as regards the out-of-plane dynamics of the pipeline that originate mainly from the Coriolis effects.
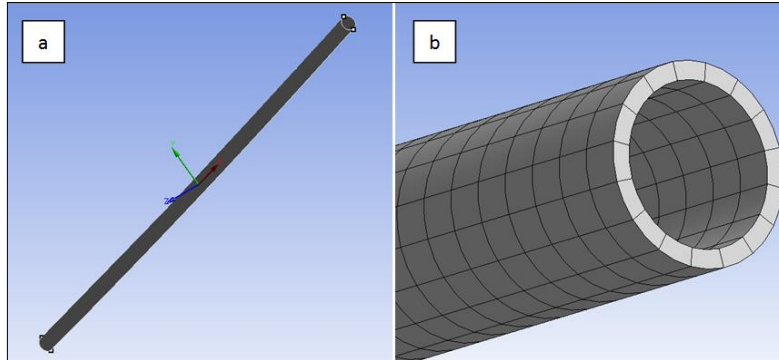
Fig. 1 Design and discretization of a tubular part with planar shells: (a) full in-plane view of the part and
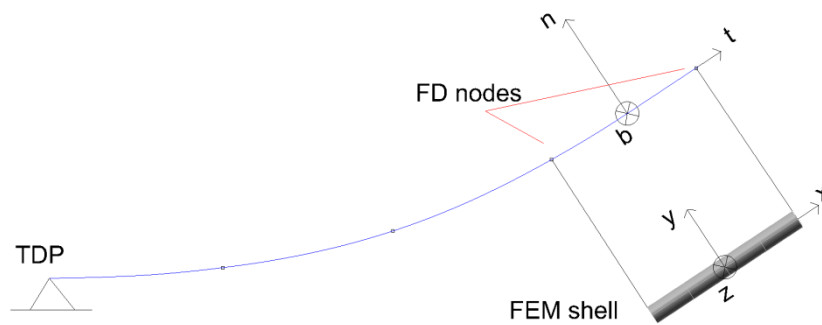(b) partial view of the mesh

Fig. 2 In-plane view of the lower sagbend region of the pipeline: Distinction between the local, Cartesian
coordinate system fixed on a tubular section of the sagbend region of the FE model (**x, y, z**) and the
one of the FD line-dynamics model (**t, n, b**); *s* denotes the unstretched Lagrangian coordinate that
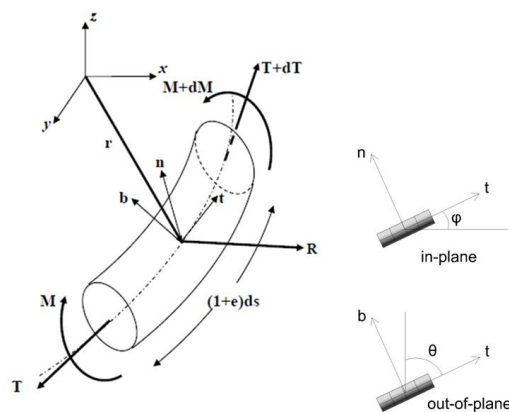takes values along the catenary

Fig. 3 Equilibrium of forces and moments on the pipe-element of the FD line-dynamics model. In-plane
and out-of-plane inclination angles

Let m, m_a and w_0 denote respectively the mass, the added mass and the submerged weight per unit length of the structure. Further, let E be the Young's modulus of elasticity, D the outer diameter, d_I the inner diameter, A the cross sectional area, I_p the polar moment, I the second moment of the pipe, ρ_c material's density and G the shear modulus. It should be noted that the quantities m, m_a, w_0, A, I and I_p correspond to the unstretched condition. Having defined the physical and the mechanical properties of the investigated structural model we provide in the following the mathematical formulation that governs its dynamic equilibrium. The equilibrium is assumed at the stretched differential element (see the schematic of Fig. 3) and the final relations are expressed in terms of the unstretched counterparts. In particular, considering the pipeline as a curved elastica it can be shown that its dynamic behavior in 3D space including torsional effects can be fully described by the following system of PDEs (Chatjigeorgiou 2013)

$$\frac{\partial T}{\partial s} + S_b \Omega_2 - S_n \Omega_3 - w_0 \sin\phi\cos\theta - m\frac{\partial u}{\partial t} - mw\left(\frac{\partial\theta}{\partial t}\cos\psi + \frac{\partial\phi}{\partial t}\cos\theta\sin\psi\right)$$
$$+ mv\left(\frac{\partial\phi}{\partial t}\cos\theta\cos\psi - \frac{\partial\theta}{\partial t}\sin\psi\right) + R_{dt} = 0 \tag{1}$$

$$\frac{\partial S_n}{\partial s} + \Omega_3 T - \Omega_1 S_b - w_0 \cos\phi - m\frac{\partial v}{\partial t} - mu\left(\frac{\partial\phi}{\partial t}\cos\theta\cos\psi - \frac{\partial\theta}{\partial t}\sin\psi\right)$$
$$+ mw\left(\frac{\partial\psi}{\partial t} - \frac{\partial\phi}{\partial t}\sin\theta\right) + R_{dn} = 0 \tag{2}$$

$$\frac{\partial S_b}{\partial s} + \Omega_1 S_n - \Omega_2 T - w_0 \sin\phi\sin\theta - m\frac{\partial w}{\partial t} - mv\left(\frac{\partial\psi}{\partial t} - \frac{\partial\phi}{\partial t}\sin\theta\right)$$
$$+ mu\left(\frac{\partial\theta}{\partial t}\cos\psi + \frac{\partial\phi}{\partial t}\cos\theta\sin\psi\right) + R_{db} = 0 \tag{3}$$

$$\frac{\partial u}{\partial s} + \Omega_2 w - \Omega_3 v - \frac{1}{EA}\frac{\partial T}{\partial t} = 0 \tag{4}$$

$$\frac{\partial v}{\partial s} + \Omega_3 u - \Omega_1 w - \frac{\partial\phi}{\partial t}\cos\theta\cos\psi + \frac{\partial\theta}{\partial t}\sin\psi = 0 \tag{5}$$

$$\frac{\partial w}{\partial s} + \Omega_1 v - \Omega_2 u + \frac{\partial\theta}{\partial t}\cos\psi + \frac{\partial\phi}{\partial t}\cos\theta\sin\psi = 0 \tag{6}$$

$$GI_p\frac{\partial\Omega_1}{\partial s} - \rho_c I_p\left(\frac{\partial^2\psi}{\partial t^2} - \frac{\partial^2\phi}{\partial t^2}\sin\theta - \frac{\partial\phi}{\partial t}\frac{\partial\theta}{\partial t}\cos\theta\right) = 0 \tag{7}$$

$$EI\frac{\partial\Omega_2}{\partial s} + (GI_p - EI)\Omega_1\Omega_3 - S_b - \rho_c I\left(\frac{\partial^2\theta}{\partial t^2}\cos\psi - \frac{\partial\theta}{\partial t}\frac{\partial\psi}{\partial t}\sin\psi\right.$$
$$\left. + \frac{\partial^2\phi}{\partial t^2}\cos\theta\sin\psi - \frac{\partial\phi}{\partial t}\frac{\partial\theta}{\partial t}\sin\theta\sin\psi + \frac{\partial\phi}{\partial t}\frac{\partial\psi}{\partial t}\cos\theta\cos\psi\right) = 0 \tag{8}$$

$$EI\frac{\partial \Omega_3}{\partial s} + (EI - GI_p)\Omega_1\Omega_2 + S_n - \rho_c I\left(\frac{\partial^2 \phi}{\partial t^2}\cos\theta\cos\psi - \frac{\partial \phi}{\partial t}\frac{\partial \theta}{\partial t}\sin\theta\cos\psi\right.$$

$$\left. -\frac{\partial \phi}{\partial t}\frac{\partial \psi}{\partial t}\cos\theta\sin\psi - \frac{\partial^2 \theta}{\partial t^2}\sin\psi - \frac{\partial \theta}{\partial t}\frac{\partial \psi}{\partial t}\cos\psi\right) = 0 \tag{9}$$

$$\frac{\partial \psi}{\partial s} - \frac{\partial \phi}{\partial s}\sin\theta - \Omega_1 = 0 \tag{10}$$

$$\frac{\partial \theta}{\partial s}\cos\psi + \frac{\partial \phi}{\partial s}\cos\theta\sin\psi - \Omega_2 = 0 \tag{11}$$

$$\frac{\partial \phi}{\partial s}\cos\theta\cos\psi - \frac{\partial \theta}{\partial s}\sin\psi - \Omega_3 = 0 \tag{12}$$

The dynamic system of Eqs. (1)-(12) has been expressed in terms of the local coordinate system (**t**, **n**, **b**) of the Frenet frame for a space curve (see Hildebrand 1976), where **t** is tangent to the axis, **n** is perpendicular to **t** and **b** is defined such that the system of vectors is orthogonal and right handed. The unknowns of the problem compose the associated vector

$$\mathbf{Y} = \begin{bmatrix} T & S_n & S_b & u & v & w & \Omega_1 & \Omega_2 & \Omega_3 & \psi & \theta & \phi \end{bmatrix}^{\mathbf{T}} \tag{13}$$

in which T denotes the effective tension, S_n and S_b are the shear forces in normal **n** and bi-normal **b** directions, u, v and w are the axial, normal and bi-normal structural velocities respectively, Ω_1, Ω_2 and Ω_3 define the torsional, the out-of-plane and the in-plane curvatures and finally, ψ, θ and ϕ, denote the Euler angles of the Frenet frame. In this particular case ψ, θ and ϕ are respectively the angle of torsion, the out-of-plane angle and the angle which is formed between the horizontal and the axis of the pipe in its 2D plane of reference. Finally R_{dt}, R_{dn} and R_{db} are the drag forces along **t**, **n** and **b** unit vectors respectively. These are taken in the form suggested by the Morison's formula, namely

$$R_{dt} = -\frac{1}{2}\pi\rho DC_{dt}u|u| \tag{14}$$

$$R_{dn} = -\frac{1}{2}\rho DC_{dn}v\sqrt{v^2 + w^2} \tag{15}$$

$$R_{db} = -\frac{1}{2}\rho DC_{db}w\sqrt{v^2 + w^2} \tag{16}$$

where ρ is the water density, whilst C_{dt}, C_{dn} and C_{db} are the associated drag coefficients. Hence the loading vectors shown in Fig. 3 are written as $\mathbf{T} = \begin{bmatrix} T & S_n & S_b \end{bmatrix}$, $\mathbf{M} = \begin{bmatrix} M_1 & M_2 & M_3 \end{bmatrix}$, where $M_1 = GI_p\Omega_1$, $M_2 = EI\Omega_2$, $M_3 = EI\Omega_3$ and $\mathbf{R} = \begin{bmatrix} R_{dt} & R_{dn} & R_{db} \end{bmatrix}$. The compatibility relation (4) implies that a linear strain relation has been considered as it was assumed that the local strain is given by $e = T/EA$.

Clearly, all above mentioned quantities are functions of the time t and the spatial unstretched Lagrangian coordinate s that takes values along the unstretched length of the pipe. In the

concerned system, Eqs. (1)-(3) are the equations of motions, Eqs. (4) and (5) represent the compatibility relations, Eqs. (7)-(9) are the balance of moments equations and finally, Eqs. (10)-(12) have been introduced artificially to construct a system of 12 equations with an equal number of unknowns. In particular, they associate the torsional and bending curvatures, or in other words the elements of the Darboux vector of rotation, with the Euler angles of the Frenet frame.

In the following we provide a brief description of the FD methodology applied for the solution of the system of Eqs. (1)-(12). Having defined the vector of the unknowns (13), the governing dynamic system that is composed by the PDEs (1)-(12) can be written according to the following matrix form

$$\mathbf{M}\frac{\partial^2 \mathbf{Y}}{\partial t^2} + \mathbf{C}\frac{\partial \mathbf{Y}}{\partial t} + \mathbf{B}\frac{\partial \mathbf{G}}{\partial t}\frac{\partial \mathbf{Y}}{\partial t} + \mathbf{K}\frac{\partial \mathbf{Y}}{\partial s} + \mathbf{F} = 0 \tag{17}$$

In the above matrix equation $\mathbf{M}$, $\mathbf{C}$, $\mathbf{B}$, $\mathbf{G}$ and $\mathbf{K}$ are 12×12 square matrices and $\mathbf{F}$ is a 12×1 column vector. The exact forms of the matrices and the vector can be found in Chatjigeorgiou (2013). This system is solved using an appropriate combination of Finite Difference schemes. Similar systems have been solved in the past using the indefinitely stable, second-order accurate $O(\Delta t^2)+O(\Delta s^2)$ implicit Keller-Box method (Hoffman 1993), where the partial differential equations of the governing system are evaluated at the middle of two successive temporal and spatial nodes, i.e., at $i+1/2$ and $k-1/2$, where i and k denote respectively the temporal and the spatial nodes. However, this method cannot be employed in the equations that involve a second-order time derivative, namely Eqs. (7)-(9). Hence these equations are treated using the Crank-Nicolson scheme (Hoffman 1993). The stencils of the employed FD schemes are shown in Fig. 4. According to the Crank Nicolson method the spatial derivatives are evaluated at the grid point [i, $k-1/2$] via the second-order centered-difference scheme. The order of this approximation is expected to be $O(\Delta s^2)$. The second-order time derivatives at spatial nodes $k-1$ and k are approximated by the second-order centered-difference estimates. The resulting finite difference approximations of Eq. (17) using the Keller-Box and the Crank-Nicolson schemes are given respectively by the following expansions.
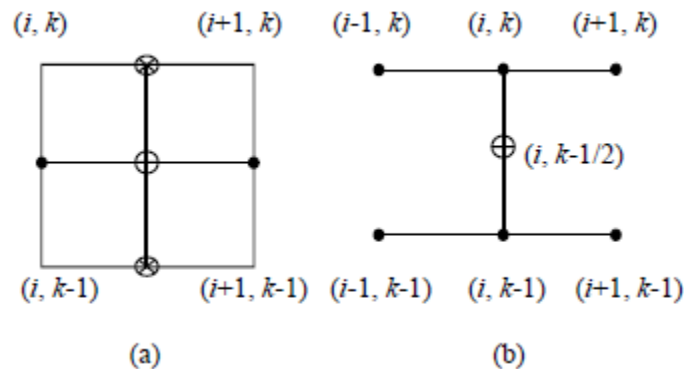

Fig. 4 Stencils of (a) the Keller-Box method and (b) the Crank-Nicolson method

$$\left(\mathbf{C}_k^{i+1} + \mathbf{C}_{k-1}^{i+1} + \mathbf{C}_k^{i} + \mathbf{C}_{k-1}^{i}\right)\left(\mathbf{Y}_k^{i+1} - \mathbf{Y}_k^{i} + \mathbf{Y}_{k-1}^{i+1} - \mathbf{Y}_{k-1}^{i}\right)\Delta s$$

$$+\left(\mathbf{K}_k^{i+1} + \mathbf{K}_{k-1}^{i+1} + \mathbf{K}_k^{i} + \mathbf{K}_{k-1}^{i}\right)\left(\mathbf{Y}_k^{i+1} + \mathbf{Y}_k^{i} - \mathbf{Y}_{k-1}^{i+1} - \mathbf{Y}_{k-1}^{i}\right)\Delta t \tag{18}$$

$$+2\left(\mathbf{F}_k^{i+1} + \mathbf{F}_{k-1}^{i+1} + \mathbf{F}_k^{i} + \mathbf{F}_{k-1}^{i}\right)\Delta t \Delta s = 0$$

$$8\left(\mathbf{M}_k^{i+1} + \mathbf{M}_k^{i-1} + \mathbf{M}_{k-1}^{i+1} + \mathbf{M}_{k-1}^{i-1}\right)\left(\mathbf{Y}_k^{i+1} + \mathbf{Y}_{k-1}^{i+1} - 2\mathbf{Y}_k^{i} - 2\mathbf{Y}_{k-1}^{i} + \mathbf{Y}_k^{i-1} + \mathbf{Y}_{k-1}^{i-1}\right)\Delta s$$

$$+\left(\mathbf{B}_k^{i+1} + \mathbf{B}_k^{i-1} + \mathbf{B}_{k-1}^{i+1} + \mathbf{B}_{k-1}^{i-1}\right)\left(\mathbf{G}_k^{i+1} + \mathbf{G}_{k-1}^{i+1} - \mathbf{G}_k^{i-1} - \mathbf{G}_{k-1}^{i-1}\right)\left(\mathbf{Y}_k^{i+1} + \mathbf{Y}_{k-1}^{i+1} - \mathbf{Y}_k^{i-1} - \mathbf{Y}_{k-1}^{i-1}\right)\Delta s \tag{19}$$

$$+8\left(\mathbf{K}_k^{i+1} + \mathbf{K}_k^{i-1} + \mathbf{K}_{k-1}^{i+!} + \mathbf{K}_{k-1}^{i-1}\right)\left(\mathbf{Y}_k^{i+1} + \mathbf{Y}_k^{i-1} - \mathbf{Y}_{k-1}^{i+1} - \mathbf{Y}_{k-1}^{i-1}\right)\Delta t^2$$

$$+16\left(\mathbf{F}_k^{i+1} + \mathbf{F}_k^{i-1} + \mathbf{F}_{k-1}^{i+1} + \mathbf{F}_{k-1}^{i-1}\right)\Delta t^2 \Delta s = 0$$

The final system is solved using the relaxation method (Press *et al*. 1986).

3.2 Solution of the FD model

At first a single top-end applied oscillation of the investigated catenary (see Section 2), of equal amplitudes, $X_a = Y_a = Z_a = 2$ m along the axes of the Cartesian coordinate system fixed at the point of attachment has been modeled within the FD solver. The phasing between the excitation components was assumed to be zero and the excitation frequency equal to $\omega = 1$rad/s. The total time of the cyclic motions which corresponds with the simulation interval was 32 periods of top-end oscillations. For the employment of the "line-dynamics" approximation via the implementation of the FD methodology, the suspended length of the catenary was spatially discretized by 101 equally spaced nodes. The time step for the simulation was taken equal to $\Delta t = 0.2$s.

In Figs. 5-8 there are some indicative results for the time variation of the internal loading components and the velocities at specified locations along the catenary. Similar loading conditions have been tracked and extensively analyzed in previews efforts (Chatjigeorgiou 2010a, Katifeoglou and Chatjigeorgiou 2012). According to the depicted time histories the expected steady state condition of the forced excitation is established at the third period onwards. The occurrence of the superharmonics at the maxima and minima of the time series of the effective tension (Fig. 7) is clearly a contribution due to the nonlinear terms. The shear force (see Fig. 8) is small compared to the axial tension. Nevertheless it should be noted that the shear force performs larger amplitudes along the sagbend and, especially, close to the TDP. The latter remark yields an expectation for large, local in-plane bending and shear stresses at the vicinity of the TDP using the FE analysis. In addition, the output signals of the shear force between successive nodes are relatively asynchronous and show largely variant amplitudes. Moreover, the axial (Fig. 5) and the normal velocity components (Fig. 6) manifest a systematically increasing trend towards the excited top-end, as it should be expected. Apparently the normal component does not vary

significantly along the higher-suspended structure contrary, once again, to the lower – close to the TDP – region. It should be mentioned that the normal motions at the lower portion of the structure imply also a significant variability of the local bending and the shear stress state.
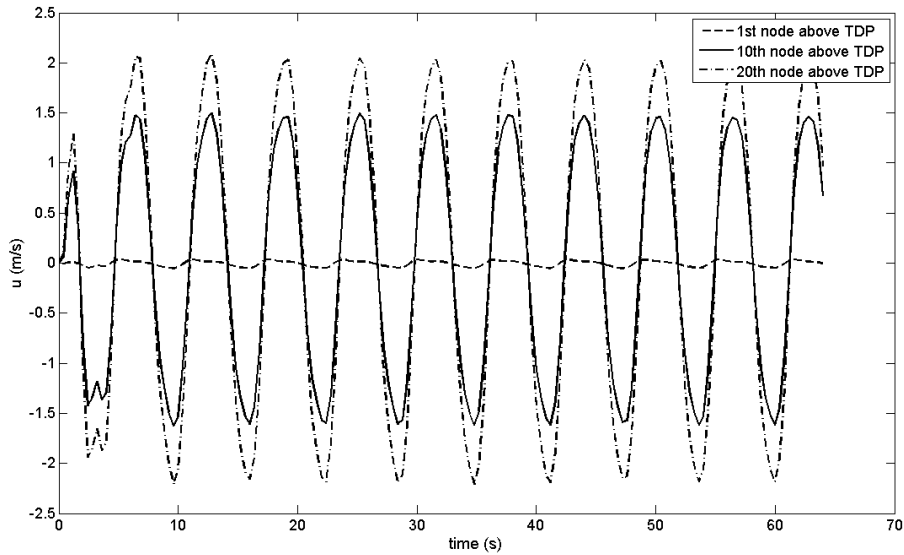

Fig. 5 Time series of the axial velocity component (with respect to the local Lagrangian, moving coordinate system) at three selected nodes along the sagbend region at s=23.762 m, s=237.62 m and s=475.24 m, accordingly
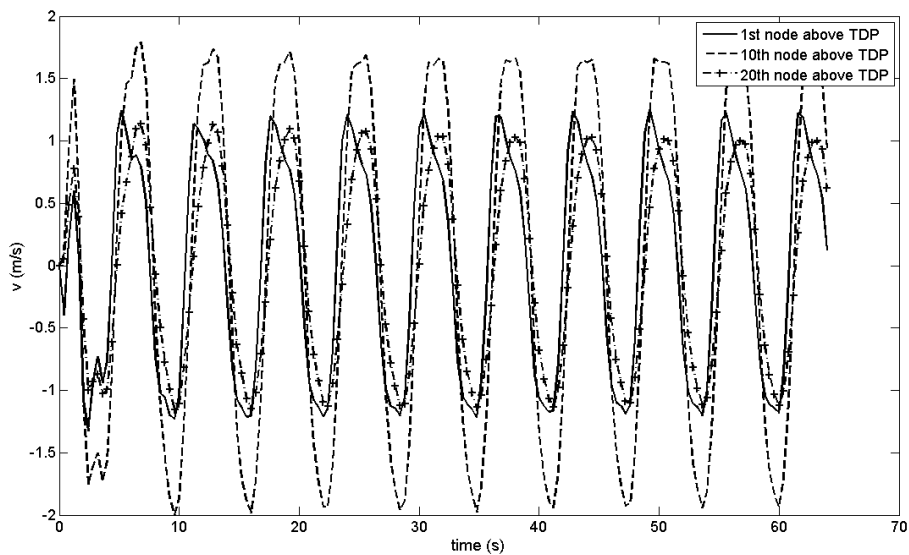

Fig. 6 Time series of the normal velocity component (with respect to the local Lagrangian, moving coordinate system) at three selected nodes along the sagbend region at s=23.762 m, s=237.62 m and s=475.24 m, accordingly
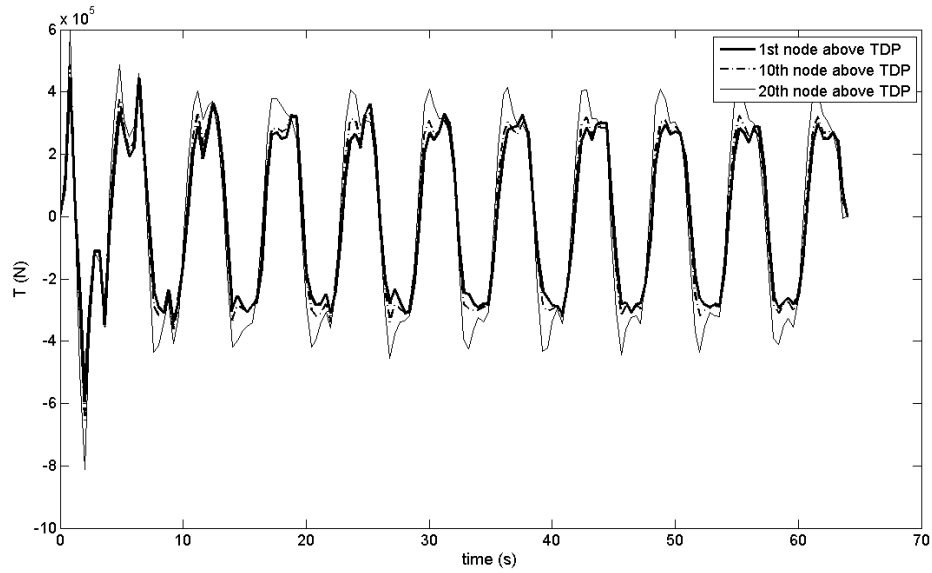
Fig. 7 Time series of the effective tension (with respect to the local Lagrangian, moving coordinate system) at three selected nodes along the sagbend region at *s*=23.762 m, *s*=237.62 m and *s*=475.24 m, accordingly
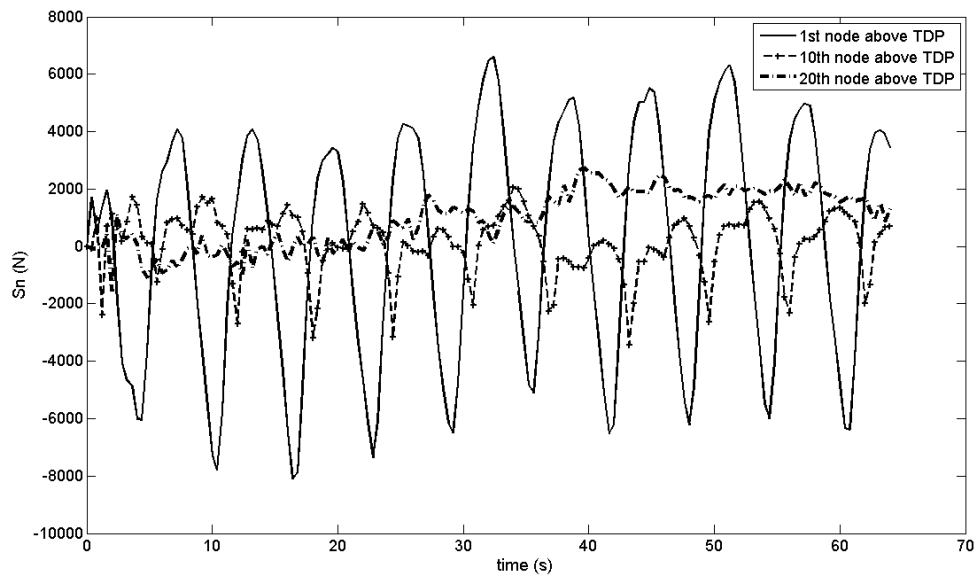

Fig. 8 Time series of the in-plane shear force S_n (with respect to the local Lagrangian, moving coordinate system) at three selected nodes along the sagbend region at *s*=23.762 m, *s*=237.62 m and *s*=475.24 m, accordingly

3.3 Design of the FE model

The design of the geometry, the mesh and the introduction of the kinematic and load conditions, have been performed as follows (see Fig. 2): (i) each part extends between two successive nodes of the FD model; (ii) a simple (hinged) support is applied at the TDP's lower edge; (iii) the FD kinematic and internal loading results for the first node above the TDP (i.e., for $k=2$) are set as input conditions for the first FE part; (iv) accordingly, all successive FD results are introduced as input conditions for the corresponding successive sections. There is a total number of 25 parts attached to each other which assemble the complete sagbend region of the structural model. As previously highlighted, the FE analysis focus explicitly in this area in which the strongest vibrations are encountered.

The time series of the internal loading terms are applied at the two end-edges of each shell-like section to secure its dynamic equilibrium. Such time varying loads apparently, cause a variable intensive condition. At the same time, a space velocity vector is applied on the investigated section. Again the velocity vector was obtained via the FD "line-dynamics" methodology. Finally the solution of the dynamic equilibrium problem of the translational shell parts is performed by the FE algorithm outlined in Section 2. The total simulation time for each of the numerical tests (corresponding to each of the 25 tubular sections) was 19.2s, which is slightly above the interval corresponding to three periods of excitation. It is reminded herein that the three periods time interval was the remarkable time required to achieve a steady state response (see e.g., Figs. 5-7). For the temporal discretization and in order to comply with ANSYS (2007) benchmarks for the "selection of a piecewise initial time step", Δt was set equal to 0.0045s.

4. Validation of the FE model

Prior to the numerical simulations to highlight the details of the dynamic response of the 25 shell-like sections that assemble the complete sagbend region, a limited number of analyses were carried out explicitly dedicated to the first section (between nodes $k=1$ and $k=2$) which is the closest to the TDP. The associated calculations were performed for validating the current approach. First, two relatively extended (80s) numerical simulations were performed for different shell elements: (i) 4-node shell elements and (ii) 8-node shell elements aiming to examine the adequacy of each discretization to describe properly the sought normal and shear stress distributions. As already mentioned in Section 2, the 8-node shells are preferred for the nonlinear analysis of thick shell structures like the one examined in the present. For validating the efficacies of the 4-node and the 8-node shell elements and justifying why the latter were finally preferred, Fig. 9 is provided, which depicts indicative time histories of the maximum dynamic von Mises stresses for both element types. It is immediately apparent that for an extended time interval, up to 40s, there is an overall similar behavior of the depicted von Mises stresses for both element types, while the 4-node shells result in generally higher peaks. After that point, the results obtained through the 4-node and the 8-node approximations clearly disagree. In particular the 8-node shell stresses tend to converge efficiently whilst the 4-node approximation is clearly divergent.

The employed FE approach was validated against the results of the FD "line-dynamics" approximation according to the following procedure. The FD solution method assumes by default that the structure is slender and hence the obtained internal loading components can be regarded as point loadings. In the same sense the produced stresses should be considered uniform, namely

having an equal value in all finite elements of the cross section. Thus, this uniform stress distribution can be determined quantitatively by taking the ratio between the force and the overall cross sectional area, which according to the Euler-Bernoulli beam formulation is constant along the pipeline. The generalized FE approximation however requires to consider the general condition of the non-uniform distribution of stresses. To validate the FE approach the stresses obtained by the FE solution were integrated over the cross sectional area providing a single force component which accordingly was transformed into the equivalent uniform stress by simply dividing by the sectional area. The latter "uniform" load was finally compared against the associated prediction of the FD "line-dynamics" solution. Indicative results for the axial (normal to the section) stresses obtained through both approaches are showing in Fig. 10. Given the inevitable differences of the two numerical methods and taking into account that the distribution of stresses obtained by the FE solution was converted into a single loading component, it can be said that the numerical predictions of the depicted, relatively extended time interval, are roughly equivalent. Undoubtedly, a single loading component can be effectively derived by the FD approach. This however does not answer crucial questions on the actual distribution of stresses which are responsible for 3D effects on the shell.

5. FE results

The snapshots in Figs. 11 and 12 depict instantaneous configurations which represent the dynamic response for two tubular sections (out of the 25) along the sagbend region of the investigated catenary pipeline. The figures show the orientations of the concerned sections at several time steps within the 19.2s simulation interval. For display reasons the snapshots are restricted on the 2D plane of reference albeit the excitation incorporates out-of-plane components. It can be immediately apparent that the out-of-plane excitations are small compared to the in-plane components, as expected. The first snapshots (upper-left) in both figures are the benchmark positions that correspond to the static equilibrium position (at t=0) in which the local Cartesian coordinate system coincides with the local ($\mathbf{t}$, $\mathbf{n}$, $\mathbf{b}$) Lagrangian system. As the dynamic phenomenon evolves, the moving Lagrangian system and subsequently the pipe-section is detached from its original (at t=0) position. In particular Fig. 11 corresponds to the 13th tubular section which is close to the middle of the sagbend region (at s=297.025 m), whilst Fig. 12 show the respective snapshots for the last tubular section at the end of the sagbend (at s=594.05) where the pipeline becomes straight and nearly vertical. In addition, it can be easily deduced that the strongest vibrations of the sagbend can be encountered at the middle of its length and that is demonstrated by the instantaneous orientations of the segment in Fig. 11. It should be mentioned that analogous heavy vibrations were observed for sections closer to the TDP. The concerned part of the segment performs translational displacements and rotational motions around the bi-normal axis. Apparently there are no significant axial displacements occur and the planar dynamic behavior of the shell element, and accordingly of the pipeline, is governed by its normal motions and the plane rotations. Indeed the latter are significantly large as it is demonstrated e.g., by the nearly 90$^\text{o}$ rotation (with respect to the original position) at 8.5s and the nearly horizontal placement at 17.1s (see Fig. 11). As expected the oscillations are reduced at the end of the sagbend region, where the pipeline admits a nearly vertical configuration (Fig. 12). This can be traced back to the larger tension force applied at that area, which acts as a restraining mechanism as regards the expected vibrations. Also, it must be underlined that the motions of the shell elements do not

follow the periodicity of the excitation. This is clearly the outcome of the strong nonlinear characteristics of the concerned dynamic system.
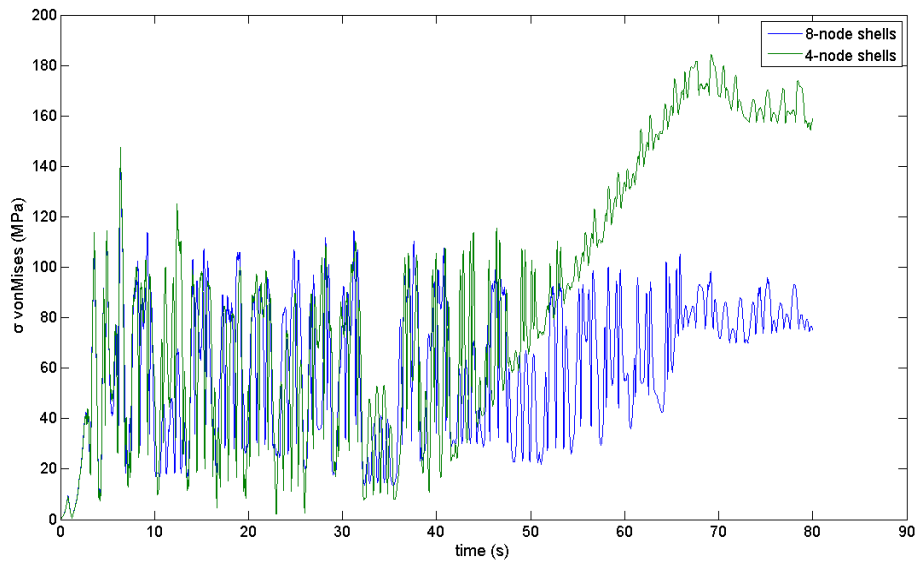

Fig. 9 Time series of the maximum von Mises stresses on the surface of the first tubular section along the sagbend region (out of 25), the middle of which is located at *s*=23.762 m
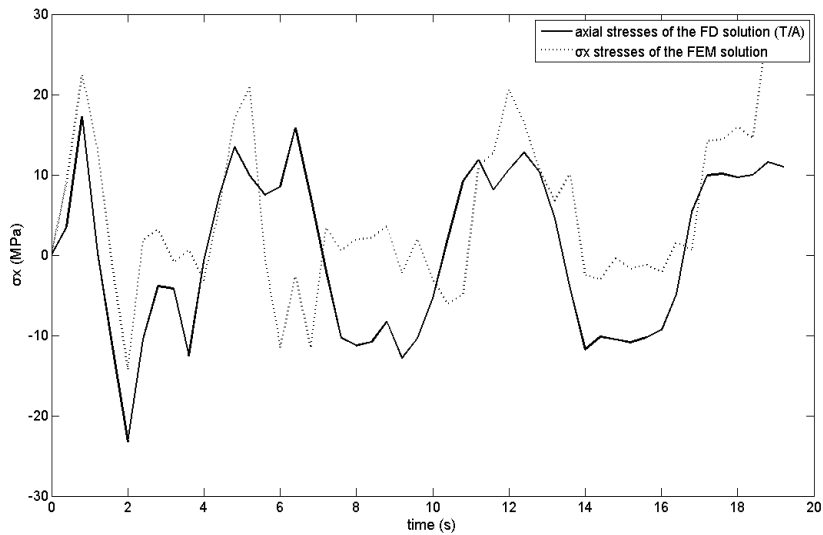

Fig. 10 Time series of axial stresses on the right edge of the first tubular section along the sagbend region (out of 25), the middle of which is located at *s*=23.762 m, using both numerical approaches. On the left edge the values are opposite
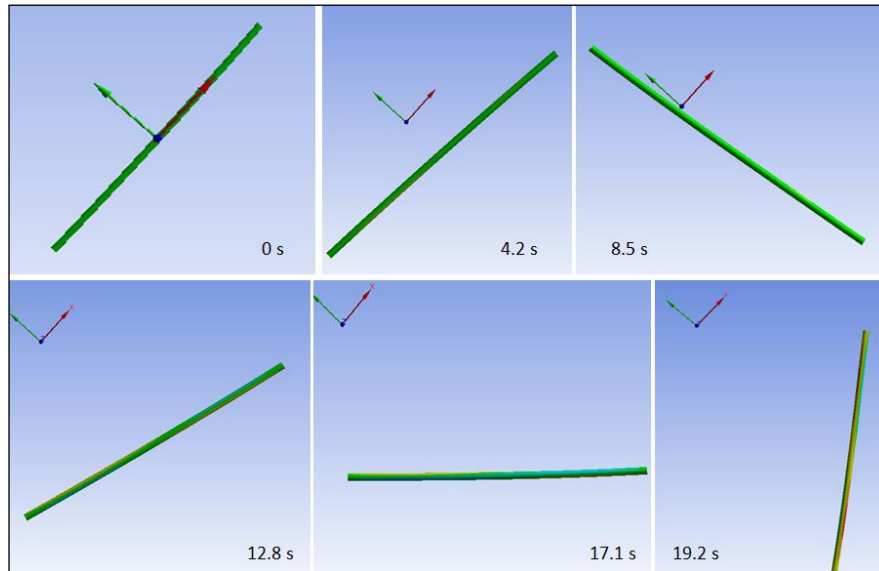
Fig. 11 Snapshots of the instantaneous orientations of the 13th tubular section along the sagbend region (out of 25) the middle of which is located at *s*=297.025 m. The depicted axes correspond to the local Cartesian system fixed on the middle of the segment at the original static position (at *t*=0)
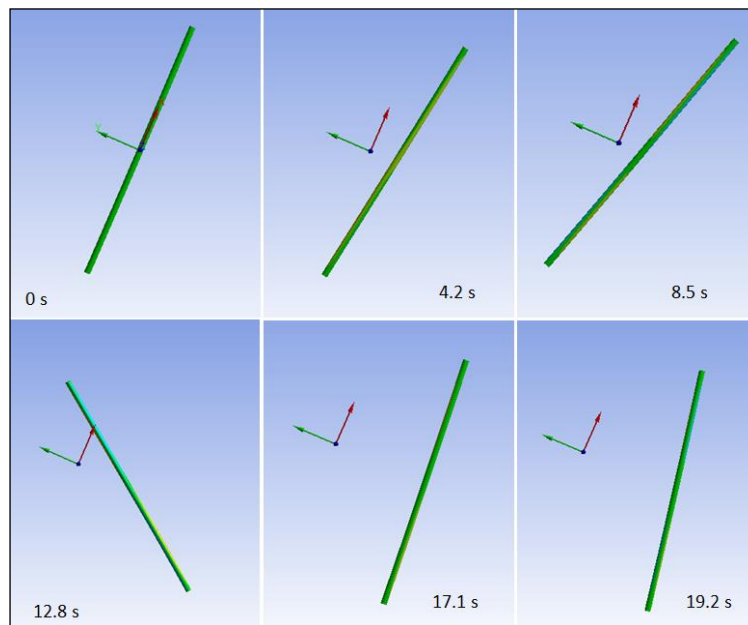

Fig. 12 Snapshots of the instantaneous orientations of the 25th tubular section along the sagbend region (the terminal segment) the middle of which is located at s=594.05 m. The depicted axes correspond to the local Cartesian system fixed on the middle of the segment at the original static position (at *t*=0)

The next series of snapshots (Fig.13) depict a more clear, perspective view of the evolution of shear stresses σ_{yz} for the 16th part along the sagbend with respect to the local Cartesian (immovable) coordinate system. It can be clearly deduced that the maximum stresses occur at the end of the third period of excitation (18.8s-19.2s). The same has been tracked for the rest stress components (σ_x, σ_y, σ_z, σ_{xy}, σ_{zx}) as well. The presented herein shear stresses are originated by the external pressure and the local bending loads and along with the bending normal stresses, σ_y and σ_z are directly connected with buckling-like fatigue of marine pipelines. The most common shape of lateral and/or shear buckling deformation of similar-task structures is the "ovalization" of the initially circular cross-section (see e.g., Kyriakides and Corona 2007). Indeed according to the depicted results, the calculations demonstrate the possibility for the occurrence of "ovalization". At the beginning of the phenomenon, the structure (here represented by a single shell element) remains undeformable and the nonzero stress distribution is attributed to the static loading. However, as the dynamic phenomenon evolves, the distribution of the concerned shear stresses is modified, mainly at the edges of the element and at the end of the investigated interval (when the steady condition is established) the pattern of the distribution of stresses is transformed throughout the shell surface (see in Fig. 14 the snapshot corresponding to 19.2s). It should be noted that the shear stresses σ_{yz} are applied normal to the depicted surface. Hence, according to the colormap in Fig. 14, there are opposite stress distributions which are concentrated on the edge of the shell and evidently, they imply potential occurrence of "ovalization".
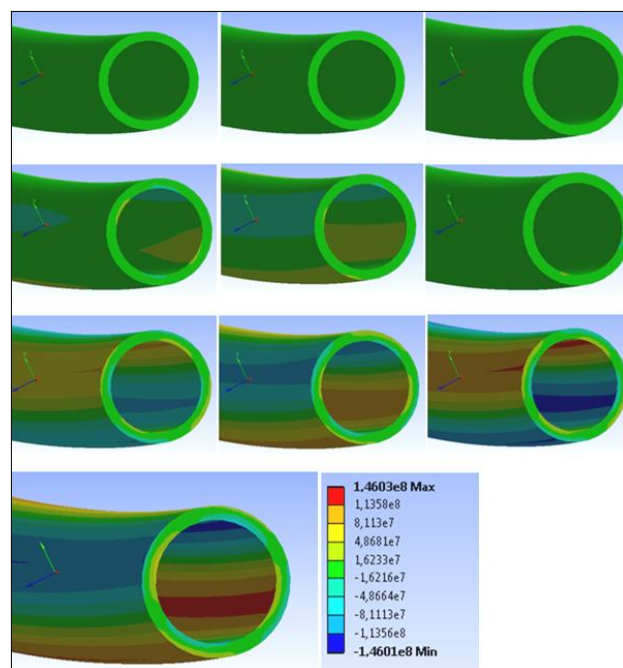

Fig. 13 Perspective contours of the shear σ_{yz} stresses for the non-deformed configuration of the 16th tubular section along the sagbend region. The depicted axes correspond to the local Cartesian system fixed on the middle of the segment at the original static position (at *t*=0). The depicted snapshots correspond with times (s) 0, 2.1, 4.2, 6.4, 8.5, 10.7, 12.9, 15.0, 17.1, 19.2
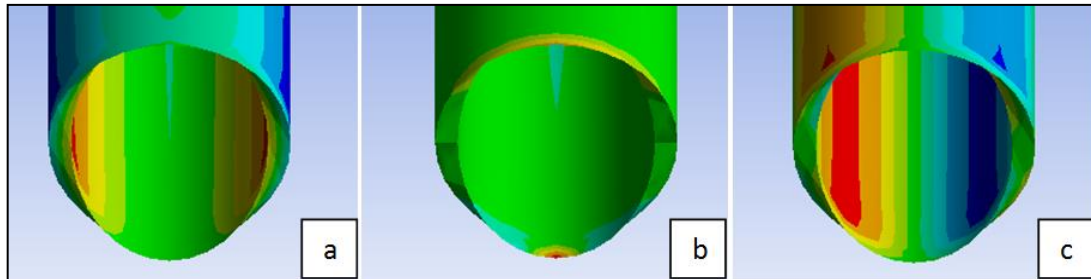
Fig. 14 Deformed contours depicting the distribution of a. normal σ_y stresses, b. normal σ_z stresses, c. shear σ_{yz} stresses (Pa) (with respect to the local Cartesian coordinate system; *y*-axis points inwards), acting on the edge of the 5th part (at the time instance of occurrence of maximum stresses, 19.0s)

Fig. 14 shows the *deformed,* "ovalized" edge contours of the same segment at the time step that corresponds to the maximum stresses (around 19.0s), with respect to the local Cartesian coordinate system. The associated pattern is primarily affected by the contribution of the maximum normal σ_y stress and much less from σ_z. The derivation of such large stress values (of hundreds of MPa) that approach limit-design values for several steel-structures, underlines the need for a limit-state control investigation, with respect to existing guidelines and recommendations. A number of limit-state analyses regarding SCRs have been performed by Estefen *et al*. (1995) and Howells (1999). Howells (1999) observed that in extreme environmental conditions the ratio of the dynamic von Mises stresses to the failure stress of the steel structure should be within the range 0.3-0.8 (the lower values should be close to TDP, since this particular location is frequently prospective for failure in extreme conditions). According to the reviews of Estefen *et al.* (1995) on the international standards on limit-state conditions for thick pipes (SCR members of *D/h*<30) the maximum permitted value for the axial-tension stress is the first yield stress of the material (in particular: 800 MPa~1 GPa). Only DetNorske Veritas introduces a factor of safety for thinner pipes (Estefen *et al.* 1995). Due to large pretensions applied on SCRs, the occurrence of large axial stresses is not an infrequent condition. However, as it was remarked in the preceding paragraphs, it is the developing cross-sectional bending and shear stress conditions which involve the largest amount of fatigue loads. For thick SCRs, the American Petroleum Institute (1998) introduces a limit value of 487 MPa under local bending stresses and a limit value 336 MPa under external pressure buckling stresses, while DNV (Estefen *et al*. 1995) defines values of similar order. The calculated maximum stresses via the employment of the FEM solution (see Fig. 16), with respect to the local-Cartesian structural system are much lower than the above limit-state values.

6. Conclusions

Nonlinear FE analyses under extended time-varying excitations were carried out for 25 shell-like parts of a catenary pipeline, discretized with 8-node planar shells. These segments assemble the sagbend region of a SCR of total suspended length 594.04 m. The transient boundary and load conditions were determined by a benchmarked FD "line-dynamics" model. The FE

solutions were in favorable agreement with the FD model predictions as regards the evolution of spatial and temporal distributions of stresses. Succinctly, the higher parts of the suspended region, of nearly vertical configuration did not perform as heavy vibrations as the lower-close to TDP, parts which corresponded with the most curved region of the pipeline. The latter remark has been evident in the celebrated shell-dynamics approximation. However, the motions of the shell elements did not follow the periodic profile of the excitations and this was attributed on one hand, due to the overall nonlinear characteristics of the particular dynamic system and on the other, due to the more complex relations involved in the discretization of the FE model. In general, the present FE-treatment's effectiveness has been highlighted for dynamic solutions of SCRs when more detailed numerical solutions than the ones derived by the usual line-dynamics approximations, are desired.

Acknowledgments

References

American Petroleum Institute (1998), Design of risers for floating production systems (FPSs) and tension leg platforms (TLPs). API-RP-2RD.

ANSYS Mechanical APDL (2007), Theory Reference Manual. ANSYS Inc.

Arabzadeh, H. and Zeinoddini, M. (2011), "Dynamic response of pressurized submarine pipelines subjected to transverse impact loads", *Procedia Eng*., **14**, 648-655.

Bathe, K.J. (1979), *Finite element formulation, modeling and solution of nonlinear dynamic problems*, Chapter in Numerical Methods for Partial Differential Equations (Ed., S.W. Parter), Academic Press.

Bathe, K.J. and Dvorkin, E. (1986), "A formulation of general shell-elements. The use of mixed interpolation of tensorial components", *Int. J. Numer. Meth. Eng*., **22**, 697-722.

Bathe, K.J. (1996), *Finite element procedures in engineering analysis*, Prentice-Hall Inc.

Chai, Y.T., Varyani, K.S. and Barltrop, N.D.P. (2002), "Three-dimensional lump-mass formulation of a catenary riser with bending, torsion and irregular seabed interaction effect", *Ocean Eng*., **29**(12), 1503-1525.

Chatjigeorgiou, I.K. (2010a), "Three dimensional nonlinear dynamics of submerged, extensible catenary pipes conveying fluid and subjected to end-imposed excitations", *Int. J. Nonlinear Mech*., **45**(7), 667-680.

Chatjigeorgiou, I.K. (2010b), "On the effect of internal flow on vibrating catenary risers in three dimensions", *Eng. Struct*., **32**(10), 3313-3329.

Chatjigeorgiou, I.K. (2013), "Numerical simulation of the chaotic lateral vibrations of long rotating beams", *Appl. Math. Comput*., **219**(10), 5592-5612.

Eom, T.S., Kim, M.H., Bae, Y.H. and Cifuentes, C. (2014), "Local dynamic buckling of FPSO steel catenary riser by coupled time-domain simulations", *Ocean Syst. Eng*., **4**(3), 215-241. DOI: 10.12989/ose.2014.4.3.215, 215-241.

Estefen, S.F., Moan, T., Saevik, S. and Zimmer, R.A. (1995), "Limit state formulations for TLP tendon and steel riser bodies", *J. Constr. Steel Res*., **32**(1), 107-121.

Hildebrand, F.B. (1976), Advanced Calculus for Applications (2nd Ed.), Prentice-Hall Inc., Englewood Cliffs, New Jersey.

Hoffman, J.D. (1993), *Numerical methods for engineers and scientists*, McGraw-Hill, New York.

Hosseini Kordkheili, S.A. and Bahai, H. (2008), "Non-linear finite element analysis of flexible risers in

presence of buoyancy force and seabed interaction boundary condition", *Arch. Appl. Mech.*, **78**(10), 765-774.

Howells, H. (1999), *FPS riser design, In: International Conference on Offshore Mechanics and Arctic Engineering (OMAE1999)*, FPS in Harsh Environments Workshop, St. Johns, Newfoundland, Canada.

Huang, H., Zhang, J. and Zhu, L. (2013), "Numerical model of a tensioner system and riser guide", *Ocean Syst. Eng.*, **3**(4), 257.273. DOI: 10.12989/ose.2013.3.4.257, 257-273.

Katifeoglou, S.A. and Chatjigeorgiou, I.K. (2012), "Dynamic interaction of catenary risers with the seafloor", *Appl. Ocean Res.*, **38**, 1-15.

Katifeoglou, S.A., Chatjigeorgiou, I.K. and Mavrakos, S.A. (2012), "Effects of fully developed turbulent internal flow on marine risers' dynamics", *Proceedings of the International Conference on Offshore and Polar Engineering (ISOPE2012)*, Rhodes, Greece.

Kyriakides, S. and Corona, E. (2007), *Mechanics of offshore pipelines. Volume 1: Buckling and collapse*, Elsevier, Oxford.

Meng, D. and Chen, L. (2012), "Nonlinear free vibrations and vortex-induced vibrations of fluid-conveying steel catenary riser", *Appl. Ocean Res.*, **34**, 52-67.

Nakhaee, A. and Zhang, J. (2010), "Trenching effects on dynamic behavior of a steel catenary riser", *Ocean Eng.*, **37**(2-3), 277-288.

Press, W.H., Flannery, B.P., Teukolsky, S.A. and Vetterling, W.T. (1986), *Numerical recipes*, Cambridge University Press.

Riveros, C.A., Utsunomiya, T., Maeda, K. and Itoh, K. (1999), "Dynamic response of oscillating flexible risers under lock-in events", *Int. J. Offshore Polar Eng.*, **19**(1), 23-30.

Subbaraj, K. and Dokainish, M.A. (1989), "A survey of direct time-integration methods in computational dynamics-II. Implicit methods", *Comput. Struct.*, **32**(6), 1371-1386.